



Local mechanical properties of dissimilar metal TIG welded joints of CoCrFeMnNi high entropy alloy and AISI 304 austenitic steel

Michael Rhode^{1,2} · Kjell Erxleben¹ · Tim Richter¹ · Dirk Schroepfer¹ · Tobias Mente¹ · Thomas Michael¹

Received: 10 November 2023 / Accepted: 7 February 2024
© The Author(s) 2024

Abstract

Multiple principal element alloys encompass the well-known high entropy alloys (HEA). The alloy system represents a new class of materials consisting of at least three alloying elements, each containing 5 to 35 at.%. Thus, this alloying concept differs fundamentally from conventional materials such as steel or nickel alloys. For this purpose, the alloying elements are specifically selected, the microstructures are adjusted in a single-phase and, in some cases, multi-phase manner. In particular, conflicting goals, such as the trade-off between strength and ductility in conventional steels, are overcome. However, in the last 20 years, the focus has been on material synthesis. With the increase in available material quantities, the focus is now on processing issues such as joining and welding processes. The weldability of HEAs has received very little attention so far. The experience with dissimilar metal welds is completely lacking but is essential for the application of these materials in combination with conventional materials. The present study presents comprehensive experimental results on the weldability of an equimolar CoCrFeMnNi-HEA in cold-rolled and heat-treated condition, which was joined by tungsten inert gas welding to an austenitic steel AISI 304. The mechanical properties of the dissimilar metal welds were characterized by cross-weld tensile samples, whereas the local deformation in the weld of the different welding zones was measured by digital image correlation. In accordance with the respective initial HEA condition (cold-rolled vs. heat-treated), the local strain behavior was divergent and influenced the global mechanical properties of both DMW types. Nonetheless, the experiments provided proof in principle of the weldability for dissimilar joints of the CoCrFeMnNi-HEA welded to conventional materials like austenitic stainless steels ensuring a corresponding capability for mechanical loading. This allows further considerations on the application of these innovative materials.

Keywords High entropy alloy · Welding · Dissimilar metal weld · Mechanical properties · Microstructure

1 Introduction

High entropy alloys (HEA) like the CoCrFeMnNi-HEA (also referred as “Cantor-alloy”) belong to the group of multiple principal element alloys. These are fundamentally different from conventional alloy systems, which usually

contain one main element, such as Fe in steel, whereas a HEA comprises several principal elements in approximately equiatomic amounts [1]. They promise excellent tunable chemical and physical properties, such as high strength and ductility, for high- and low-temperature applications [2]. In perspective, this may lead to a substitution of classical high-alloy steels or Ni-based alloys. First HEAs for joining processing are commercially available in terms of powders for additive manufacturing, like the CoCrFeMnNi-HEA [3] or a AlCrFeMnNi-HEA [4].

During the last 20 years, the quantity of HEA materials available has increased due to research efforts in material synthesis. As a result, processing issues, such as joining and welding, are becoming increasingly important. As summarized in diverse comprehensive review papers, the weldability of HEAs for fusion welding (via laser and TIG) is generally good [5–8]. Generally, dissimilar metal welds (DMWs)

Recommended for publication by Commission II—Arc Welding and Filler Metals.

✉ Michael Rhode
michael.rhode@bam.de

¹ Bundesanstalt für Materialforschung und -prüfung (BAM), Department 9 - Component Safety, Unter den Eichen 87, 12205 Berlin, Germany

² Institute for Materials Research and Joining Technology, Otto-von-Guericke University, Universitätsplatz 2, 39106 Magdeburg, Germany

Table 1 Selected results of DMW studies of CoCrFeMnNi-HEA welded to conventional materials by different welding processes [11–16]

HEA	Counterpart	Welding process	Ref
CoCrFeMnNi	Austenitic stainless steel AISI 308 (as filler material)	Gas metal arc welding	[11]
	CoCrFeMnNi (as-casted)	Laser welding	[12]
	Austenitic stainless steel AISI 304	Diffusion welding	[13]
	Austenitic stainless steel AISI 316	Laser welding	[14]
	Austenitic stainless steel AISI 304	Friction stir welding	[15]
	Duplex stainless steel	Laser welding	[16]

can come across with some metallurgical challenges like the formation of intermetallics or high residual stresses [9, 10]. But experience with DMWs of HEAs to other materials is rare so far. Table 1 gives a brief overview on literature studies of CoCrFeMnNi DMWs joined by different welding processes [11–16].

In addition, HEAs are candidate materials as welding consumables to join different materials like metal–metal or metal–ceramics [17]. First applications are, for example, the use as interconnector materials for solid oxide fuel cells (SOFC) [18]. Nonetheless, for the potential application of high-entropy materials, it is essential to investigate the weldability and related performance (e.g., mechanical or corrosion resistance) of the respective DMWs. The establishment of reliable DMWs of HEAs joined to conventional materials can ensure the integrity of the welded components as well as cost reduction effects (by multi-material-mix strategies for modern component manufacturing).

For that reason, this study presents selected results of dissimilar metal joints of CoCrFeMnNi-HEA in cold-rolled and heat-treated condition TIG welded to an austenitic stainless steel. Results are presented for the influence of the microstructure on the mechanical cross-weld properties with focus on the local strains.

2 Materials and methods

2.1 Materials investigated

An equimolar CoCrFeMnNi-HEA was used as base material (BM) as well as a commercial austenitic stainless steel type 304, using the American Iron and Steel Institute (AISI) nomenclature. Table 2 shows the chemical composition of

Table 2 Chemical composition of 304 steel and CoCrFeMnNi-HEA, element content in weight percent

Element	Co	Cr	Fe	Mn	Ni
304 steel	-	19.9	69.1	1.6	7.6
CoCrFeMnNi	19.7	20.7	19.6	20.1	19.9

the investigated materials. The HEA composition was determined by electron microprobe analysis (using JEOL JXA-8900-RL analyzer, JEOL GmbH, Germany). The 304 steel was investigated by optical emission spectroscopy (using Spectrotest analyzer, Spectro GmbH, Germany).

For the AISI 304, only the main elements are shown in Table 2. The grade additionally contained C (0.32%), Si (0.88%), and P + S (<0.07%). The CoCrFeMnNi-HEA contained small amounts of material synthesis-related impurities (Cr- and Mn-oxides in accordance with [19]). It was kindly delivered by the group of Prof. Guillaume Laplanche, Ruhr-University Bochum, Germany. The synthesis process encompassed the vacuum induction melting of elements (as powder with purity of 99.9 wt.%). The molten powders were casted to ingots with a diameter of 40 mm and homogenized at 1200 °C for 48 h. Details of the materials synthesis are described in [20]. The heat-treated ingots were cold-rolled to a thickness of 1.2 mm and cut to plates with a width of 40 mm and 75 mm length. For the welding experiments, two material conditions of the HEA were considered: (1) the initial cold-rolled (CR) condition and an (2) additional recrystallization via heat treatment (HT) of the CR-condition at 1020 °C for 1 h.

2.2 TIG welding

Tungsten inert gas (TIG) welding was performed on a Polysoude PC 600 (by Polysoude S.A.S., France) in pulsed arc mode. The welding parameters are presented in Table 3. They were adapted from HEA bead-on-plate TIG welds and presented in [21, 22]. The calculated welding heat input

Table 3 TIG welding parameters

Parameter	Unit	Value
Basic current	A	35
Peak current	A	90
Voltage	V	10
Pulse frequency	Hz	4
Welding speed	mm/min	300

was 0.13 kJ/mm (effective values of current and voltage, in accordance with [23]).

The welds were made in horizontal position (PA) using shielding gas I1-Ar (argon with gas quality 5.0; see [24]) with a flow rate of 15 l/min. In addition, a backing gas R1-ArH-7,5 (92.5% Ar and 7.5% H₂; see [24]) with 10 l/min was used for shielding of the weld root. To generate conditions as close to reality (in terms of the degree of stiffness and clamping), the weld parts (one side the HEA and the 304 steel as the counterpart) were fixed in a clamping device; details were presented in [21]. The plates were clamped within an area of 1 mm at the longitudinal edge and an approximately 70 mm weld seam was produced. The experimental setup is shown in Fig. 1. To ensure oxidization prevention of the weld joint during cooling, a tail shielding gas nozzle with I1-Ar (Ar 5.0, gas flow of 15 l/min) was mounted behind the TIG torch in welding direction. Two type K-thermocouples were attached at the weld start as well as in the center to monitor the plate temperature and for estimation of the cooling behavior of the weld joint.

2.3 Metallography, SEM, and hardness measurement

2.3.1 Sample preparation and conducted investigations

Cross-sections perpendicular to the welding direction were extracted in the center region of the welded plates. The samples were embedded in epoxy resin and ground by different SiC grinding papers to finally 2000 grit. Finally, they were polished with a diamond polishing paste to 1 μ m. To reveal the corresponding microstructures, the cross-sections were two-step etched: at first with Adler's etchant for 60 s and second by Beraha-II etchant for 15 s, both at room temperature (based on the experience presented in [22]). Light optical microscope (LOM) examinations were carried out using a POLYVAR MET microscope (from Reichert-Jung, Austria)

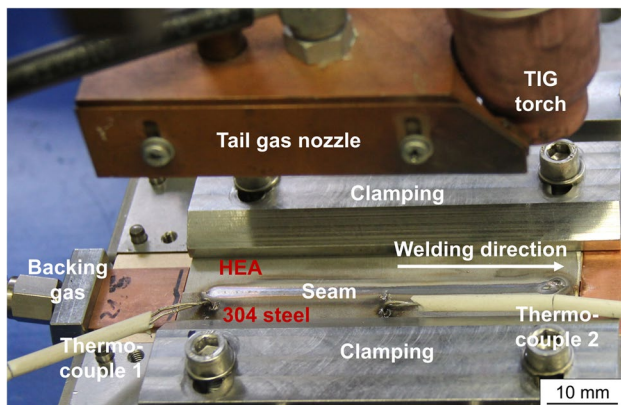


Fig. 1 TIG welding setup with clamping device

with a Gryphax-Altair camera (from Jenoptik, Germany). For acquisition of the images, the software IMS Client (from Imagic Bildverarbeitung GmbH, Germany) was used. SEM investigations of the microstructure and the fractured tensile samples (geometry shown in Fig. 2a) were carried out using a Phenom XL tabletop SEM (from Thermo Fisher Scientific).

2.3.2 Hardness measurements

The hardness measurements were conducted for the entire weld joint cross-section using an ultrasonic contact impedance (UCI) analyzer UT200 (from BAQ GmbH, Germany). UCI is characterized by a vibrating rod with a diamond pyramid attached to its tip. In accordance with [25], a microhardness determination of Vickers hardness HV0.1 was targeted. The individual measuring points had a lateral spacing of 100 μ m in x and y direction, leading to a hardness map of the entire cross-sections of the DMWs.

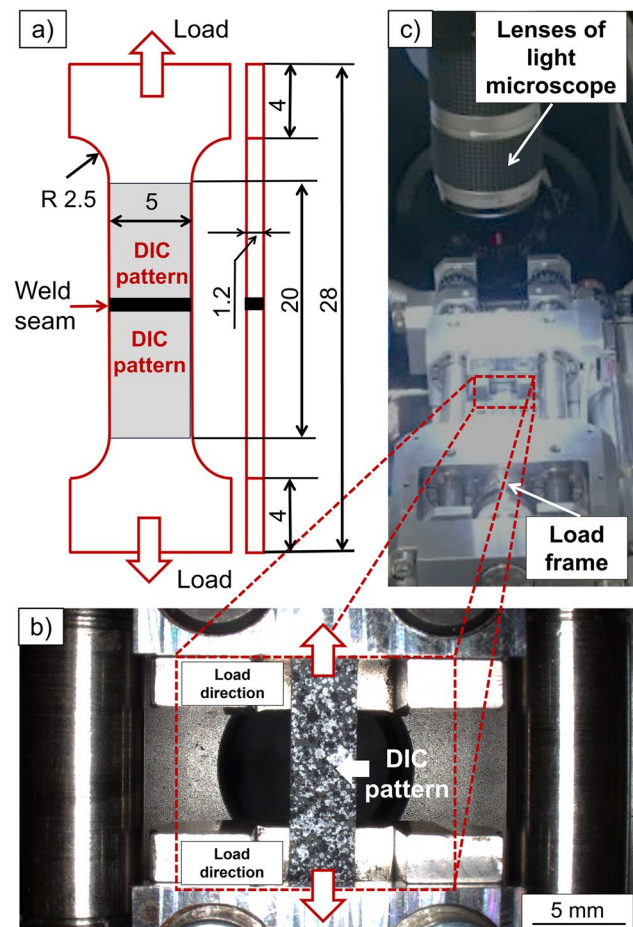


Fig. 2 Tensile sample: (a) geometry in accordance with [26], (b) detail of gage section covered with stochastic pattern, (c) mounted in loading frame under light microscope

2.4 Tensile test

Tensile tests were conducted with “dog bone”-like flat samples machined from the BMs and cross-weld samples of the corresponding DMWs with the weld seam in the center of the sample. The tensile test geometry is shown in Fig. 2a (geometry in accordance with [26]). The sample cross-section corresponded to an area of 6 mm² within the gage section, encompassing a total gage length of 20 mm.

2.4.1 Load frame and data acquisition

The test speed was set to 10 μm*s⁻¹ (displacement-controlled) using a mechanical load frame (from JPK Instruments, division of Bruker Nano GmbH, Germany), as shown in Fig. 2b and c. This speed was equivalent to a strain rate of 5 × 10⁻⁴*s⁻¹ (based on the gage length of 20 mm). Subsequently to the mounting of the sample into the loading frame, a small preload of 10 N was applied and the camera system for the in situ strain analysis checked and the data logging unit triggered. During the tensile test, the data acquisition of both the force and displacement was realized by the DDS-3 system and Measurement and Control Device Software MDS 4.0 (both from Kammrath Weiss GmbH, Germany). The welded seam of the mounted DMW sample in Fig. 2b is not directly visible because it was covered by a stochastic pattern for the measurement of the local strains, as shown in the next sub-sections.

2.4.2 Global engineering stresses and strains

The global engineering stress was obtained via the division of the measured force (in N) vs. the cross-section of the sample of 6 mm² (1.2 mm thickness × 5 mm width; see Fig. 2a). Due to the relatively small sample length within the available compact loading frame, neither a tactile could be applied nor an optical extensometer due to the mounted camera optics. For that reason, the measured cross-head displacement (in millimeters) was related to the gage length of 20 mm for the calculation of the global strain (in percent). Of course, the strain did not represent an exact value. Indeed, cross-weld samples are not applied for calculations of a certain yield strength of the welding joint due to the very heterogeneous DMW microstructures. For that reason, an approximated value for the total strain of the DMW is also of high interest for the assessment of the global straining behavior.

2.5 Measurement of local strains by DIC

Different welding microstructures can have way different local mechanical properties. To estimate which microstructure was decisive for the (necking and) failure of the sample during the tensile test, the digital image correlation (DIC)

technique was applied. This allowed the in situ identification of the local strains, e.g., in the WM and the HAZ. For that purpose, automated light microscopy images were acquired every 20 s during the tensile test by a VHX 7000 Digital Microscope (Keyence) with the lens aligned vertically above the flat tensile specimen (see Fig. 2c). The obtained row of images of the top surface of the weld joint was analyzed by the GOM Correlate software (Carl Zeiss GOM Metrology GmbH, Germany). For that purpose, each subsequent image was compared to the corresponding preceding image. The first image was obtained at “zero” loading condition (at the mentioned 10 N preload). For the strain identification via the displacement measurement, a pixel mesh was defined (edge length of the single pixel of approximately 15 μm) and applied to the acquired images of the tensile sample, encompassing the entire gage length (20 mm) and width (5 mm). Subsequently, the local strain at each respective pixel position was individually calculated as mean value of a facet defined to 25 pixels (375 μm) and a point spacing of 16 pixels (240 μm) resulting in a local strain. For strains determined by DIC, an internal deviation of ± 2% has to be considered.

The prerequisite for a precise DIC-analysis is the stochastic pattern on the specimen with a high contrast, which is necessary for the GOM software to identify (and to follow) the displacement of the sample during straining. To ensure the high-contrast, a black pattern was manually speckled on a white background, as shown in Fig. 2b. For that purpose, two black and white varnishes (supplier: Auto-K GmbH, Germany) were used ensuring both a sufficient deformation ability and an adhesion/bonding to the substrate surface. Prior tensile tests ensured that with the chosen applied test speed of 10 μm*s⁻¹, the stochastic pattern did not show significant delamination effects during the entire tensile test.

3 Results and discussion

3.1 Cross-sections and microstructures

Figure 3a shows a representative cross-section for the DMW of the cold-rolled HEA. Detailed microstructure features are shown in Fig. 3b for the HAZ of the 304 steel, Fig. 3c the HAZ of the cold-rolled HEA base material, and Fig. 3d for the intermixed WM. Figure 3e presents the DMW with the heat-treated HEA with details in Fig. 3f for the HAZ of the 304 steel, Fig. 3g the HAZ of the heat-treated HEA base material, and Fig. 3h the intermixed WM. Defect-free weld joints (e.g., pores or cracks) were ensured by visual and radiographic testing. From that point of view, the TIG welding parameters (see Table 3) based on the HEA bead-on-plate welds in [21, 22] were successfully transferred to the presented DMWs (and the TIG weldability for the dissimilar metals proofed).

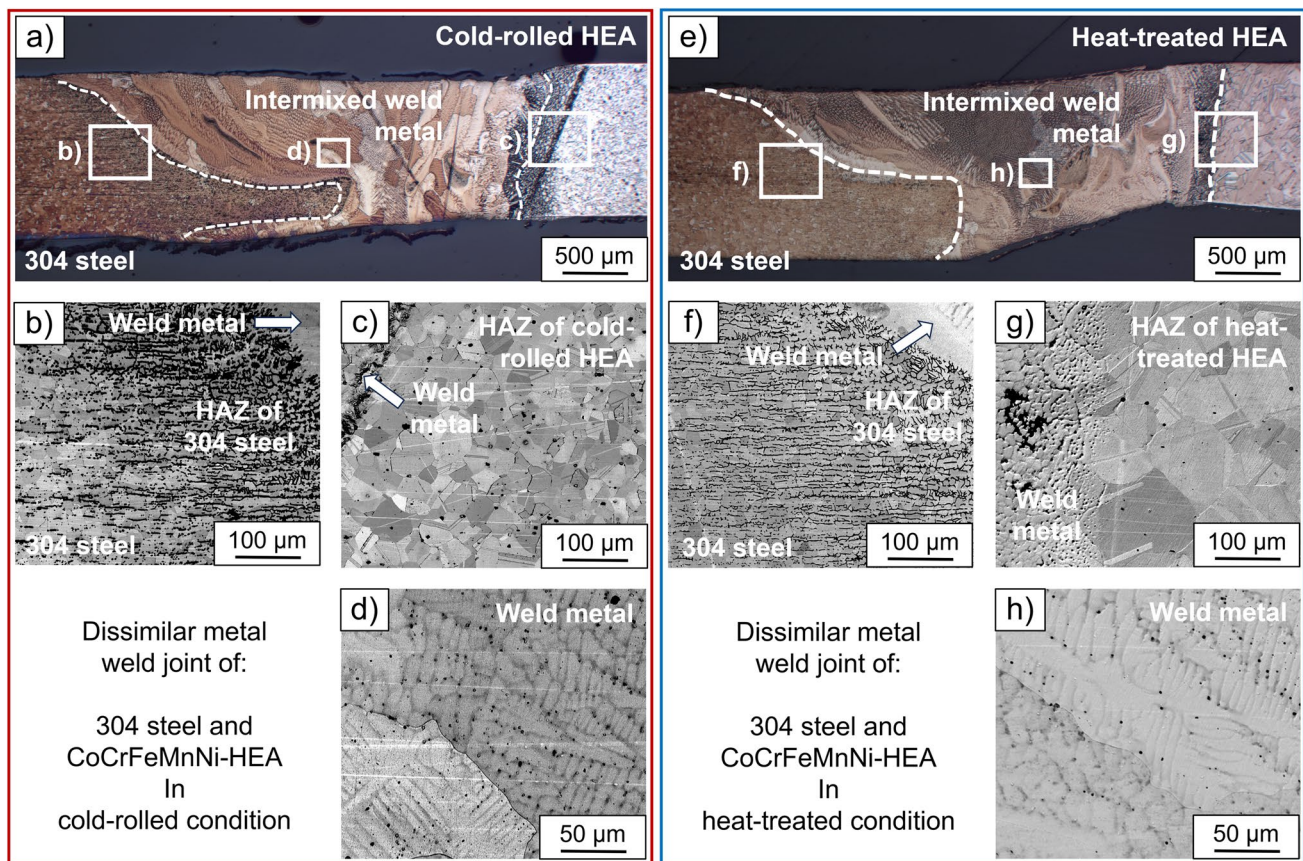


Fig. 3 Cross-section of DMWs of 304 steel welded to **a** HEA in cold-rolled condition with magnified detail of **b** HAZ of 304 steel, **c** HAZ of HEA, and **d** intermixed weld metal; **e** HEA in heat-treated condi-

tion with magnified detail of **f** HAZ of 304 steel, **g** HAZ of HEA, and **h** intermixed weld metal

For both DMWs, the intermixed WM showed a dendritic microstructure (DMW of the cold-rolled HEA in Fig. 3d and the DMW of heat-treated HEA in Fig. 3h) with some micro-segregations between the dendrites. In accordance with [27], CoCrFeMnNi-based HEA-to-HEA TIG welds showed segregation of Mn into the interdendritic regions. In addition, Fe-enriched dendrite cores were indentified as shown in [28]. In this reference, the detailed chemical analysis of the aforementioned dendrite regions is presented. Nonetheless and based on available studies on fusion welded CoCrFeMnNi-HEAs to austenitic stainless steels (see Table 1 and in accordance with [11–16]), potentially critical weld-defects like brittle intermetallic phases are unlikely to occur. The most obvious difference between the HEA in CR-condition (Fig. 3c) compared with the HT-condition (Fig. 3g) was the different grain size. The coarsening of the grains in the heat-treated HEA was exclusively related to the annealing (HT) of the cold-rolled HEA at 1020 °C for 1 h (see Sect. 2.1) prior to the welding. Considering Fig. 4 (HV-distribution), the grain size cannot be directly correlated to a change of the hardness.

According to the weld joint geometry, the macro-sections in Fig. 3a and e suggest that some inconsistencies occurred. At first, it is reasonable that due to the relatively small sheet width in combination with the well-known low thermal conductivity [5, 29], welding distortions were favored. For that reason, a geometrical offset between the different welding parts occurred after the clamping force was released, and the welding distortions were allowed to take effect. Second, the weld metal thickness was assumed to be influenced to a certain extent by the small (but unavoidable) gap between the welding parts. This could not be balanced by a HEA welding consumable (not commercially available as wire). For that reason and due to the limited availability of the HEA base materials, a possible small deviation of the weld metal thickness was not further evaluated.

3.2 Hardness

The HV0.1 DMW hardness distribution of the 304 steel welded to the cold-rolled HEA is shown in Fig. 4a and welded to the heat-treated HEA in Fig. 4b, respectively.

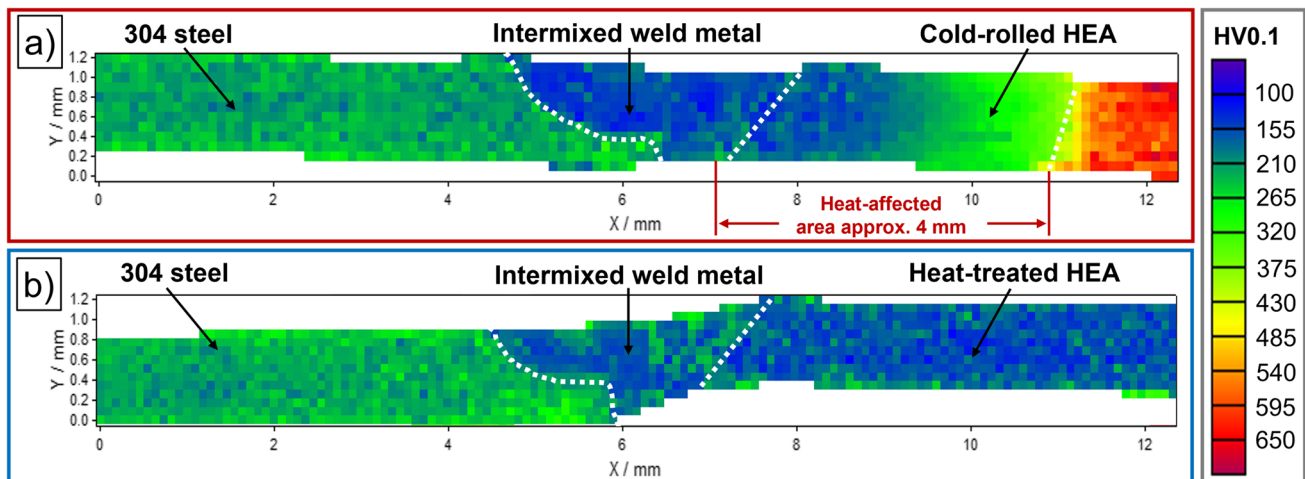


Fig. 4 Microhardness of DMWs of 304 steel welded to HEA in **a** cold-rolled and **b** heat-treated condition

Due to the geometrical small offset of the welding plates (Fig. 3), a deviation between the transverse weld joint axis and the x - y -coordinate system of the UCI analyzer occurred, especially for the weld joint with the cold-rolled HEA. For that reason, the hardness map was slightly “tilted” (see Fig. 4a).

The most significant difference in the hardness distribution was identified in the HEA. For the cold-rolled HEA, an average hardness of > 600 HV0.1 was found, whereas the HEA in the heat-treated condition had < 200 HV0.1. The 304 steel had an average hardness of 280 HV0.1. The intermixed weld metal showed for both welding conditions a significant softening, comparable to values of the heat-treated HEA. Of course, the weld heat input caused a significant decrease of the hardness of the cold-rolled HEA due to annealing effects of the microstructure. The predominant annealing effects for a CoCrFeMnNi-HEA can be attributed to the well-known annihilation of dislocations [30, 31] by recrystallization as well as texture effects known from heavily deformed austenitic TWIP steels [32]. For that reason, a strong hardness gradient was found, expressed by a drop of nearly 400 HV0.1 within a 4-mm heat-affected area (see cold-rolled HEA base material in Fig. 4a, right-hand side). The term HAZ was intentionally avoided as distinct microstructural changes did not occur [28]. The hardness decrease was merely due to the well-known annihilation of the cold-rolling effects like high number and density of dislocations. For some alloys, like Fe-based steel, the hardness and tensile strength are roughly proportional (see ASTM A 370–23 [33]). From that point of view, the weld metal region should be of special interest for the local mechanical properties as they determine the global performance of the cross-weld sample strength. For that purpose, the local strain measurements (identified by digital image correlation) are presented in the next section.

3.3 Global mechanical properties of base materials and cross-weld samples

The global mechanical tensile properties are shown in Fig. 5 as engineering stress–strain diagrams assuming a constant sample cross-section. The individually calculated ultimate tensile strength (UTS, R_m in MPa) and the maximum strain (ϵ in %) is given in Table 4. In addition, the yield strength (YS, $R_{p0.2}$ in MPa) is given for the base materials (as average value for three samples per BM-condition). For comparison, an approximated YS is given for the DMWs, although cross-weld tensile samples do not directly allow to calculate a YS (due to the heterogenous ductility of the weld joint zones, especially the HAZ).

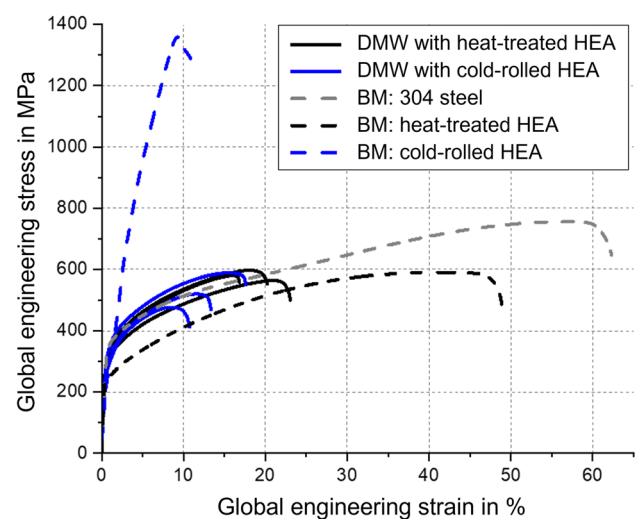


Fig. 5 Stress strain curves of base materials 304 steel, HEA in cold-rolled (CR) and heat-treated (HT) condition, and corresponding DMWs

Table 4 Overview of mechanical properties of 304 steel, HEA in cold-rolled (CR) and heat-treated (HT) condition, and corresponding DMWs (* YS derived from tensile samples, ** approximated YS from DMWs cross-weld tensile samples)

Grade	R_m in MPa	$R_{p0.2}$ in MPa	ϵ_{max} in %
304 steel	752 ± 19	$323 \pm 23^*$	62 ± 2
Cold-rolled HEA	1358 ± 70	$207 \pm 59^*$	8 ± 2
Heat-treated HEA	577 ± 30	$240 \pm 13^*$	46 ± 3
DMW with cold-rolled HEA	529 ± 56	$286 \pm 31^{**}$	13 ± 3
DMW with heat-treated HEA	580 ± 16	$286 \pm 13^{**}$	19 ± 3

As shown in Fig. 5, both the 304 steel and the HEA in HR-condition (as base materials) show the well-known high ductility of FCC-phase materials of austenitic steels [34]. As presented in Table 4, the 304 steel had a maximum strain $\epsilon_{max} = 62 \pm 2\%$ and HEA-HR had a slightly decreased maximum strain of $\epsilon_{max} = 46 \pm 3\%$. The cold-rolling of the HEA results in a significant decrease of the ductility (cold-rolled HEA to $\epsilon_{max} = 13 \pm 3\%$) but is accompanied by the expected increase of the UTS to 1358 ± 70 MPa. This is nearly 2.5 times of the UTS (577 ± 30 MPa) of the heat-treated HEA.

As a main result of this study, the DMWs generally showed a sufficient mechanical performance. In both conditions, a tensile strength of > 500 MPa as well as a (approximated) yield strength of 286 ± 31 MPa was achieved. The ductility of the DMW with the heat-treated HEA as base material was slightly better ($\epsilon_{max} = 19\%$) compared to the DMW with the cold-rolled HEA ($\epsilon_{max} = 13\%$). From the tensile data of the cross-weld DMW samples, it is reasonable to regard the CoCrFeMnNi-HEA as a potential structural material with good weldability for DMWs with austenitic steels like a 304 steel. Nonetheless, the question arises on how different materials influence the local strains of the welded joint. The reason is that the engineering stress–strain diagram only delivers a global strain across the entire weld

sample. From that point of view, the local straining during the increasing mechanical load by the tensile test is of high importance. The results are presented in the next section.

3.4 Local strains and fracture location of DMW with cold-rolled HEA

Figure 6 shows the obtained results for the local strains in the DMW of the 304 steel joined with the cold-rolled HEA. For that purpose, Fig. 6a shows a representative stress strain diagram of the respective DMW. Due to the large amount of DIC-data, Fig. 6b shows three selected representative patterns. These were selected to describe the mechanical behavior at different load/straining steps during the tensile test: step (I) within the plastic regime before UTS, step (II) at UTS, and step (III) shortly before rupture. In the DIC-patterns, the colors describe the calculated local straining (from blue with $\epsilon = 0\%$ up to red with the corresponding maximum values). For comparison reasons, the patterns of steps I to III have individual scales shown on the right of the respective pattern. It is obvious that for all three steps I to III, the weld metal had always the highest local deformation (as indicated by the red and orange colors). Compared to the global strain of 4.2% (see Fig. 6a) at step I, local strains in the intermixed WM of up to 25% were observed. The strains in the HEA as well as the 304 steel were close to the measured global strain. A comparable behavior was found at step II with the highest applied mechanical load, i.e., stresses. At this respective step, the global strain is approximately 9% and corresponds to the local strains in both BMs.

The highest global strains were found in the WM (at local spots $> 60\%$). In addition, a local higher straining can be found at the respective fusion lines and in the heat-affected area of the HEA. This is in accordance with the obtained hardness decrease from 600 HV0.1 to below 200 HV0.1. Immediately before the final rupture (step III), local WM

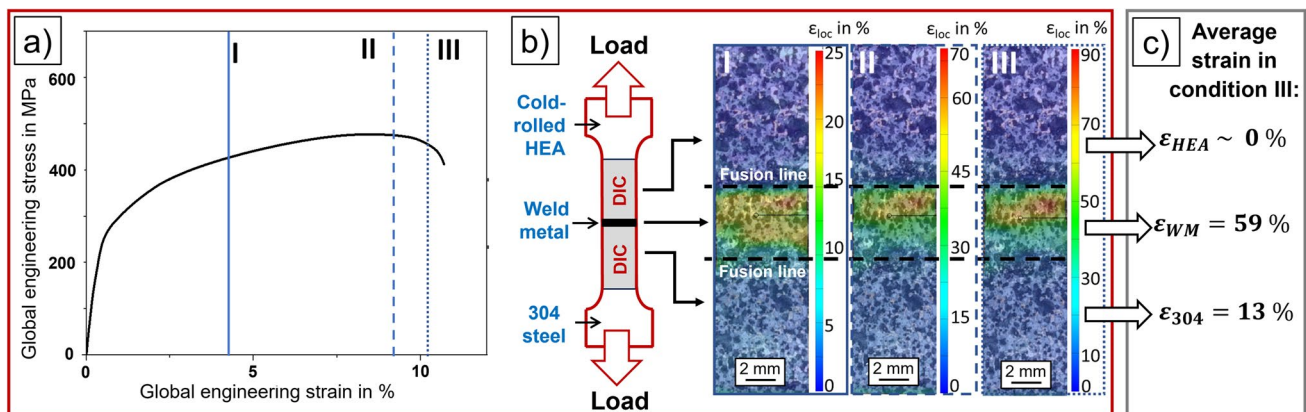


Fig. 6 Representative cross-weld tensile sample of DMW of cold-rolled HEA welded to 304 steel: **a** global engineering stress strain curve, **b** local strains at load steps I to III

strains increase at hotspots to $> 80\%$. Due to the local differences in the strains, Fig. 6c shows the averaged strains (mean value) of the BMs including the respective HAZ and the intermixed WM. In that connection, the averaged strain in the WM is higher compared to the HEA and the 304 steel. Interestingly, the averaged strain ϵ_{HEA} of the cold-rolled HEA is virtually around 0%. That means due to the high initial deformation, the mechanical tensile load is directly transferred to the intermixed WM. This can be clearly seen for all load steps I to III by the pile-up of high strains in the vicinity of the fusion line between the cold-rolled HEA and the intermixed WM (Fig. 6b), resulting in an increased average strain of $\epsilon_{WM} = 59\%$, i.e., very high deformability of the WM.

3.5 Local strains and fracture location of DMW with heat-treated HEA

Figure 7 shows the DMW of the 304 steel welded to the HEA in HT-condition. In accordance with Sect. 3.4, three different representative load steps I to III are further evaluated. If the individual BMs are regarded, it is noteworthy that due to annealing, the HEA softens. In accordance with [30, 31], an important effect of annealing in this CoCrFeMnNi-HEA is the annihilation of dislocations. This is expressed by the remarkably decreased hardness in the HEA (see Fig. 4) as well as by the increased deformability. As indicated by the different colors in Fig. 7b, the local strains range from 10 to 12% (step I) and from 12 to 18% (step II) and remain in this range (step III). The 304 steel had slightly decreased strains that compensated the local strains in the WM. They were remarkably lower compared to the WM if joined to the HEA in CR-condition. Hot spots with 18% (step I), 36% (step II), and $> 60\%$ were identified.

As shown in Fig. 7c, the average strain in the WM of the DMW with the heat-treated HEA corresponds to $\epsilon_{WM} = 41\%$ at step III. This is remarkably lower compared to the local WM ductility of $\epsilon_{WM} = 59\%$ in case of the DMW with cold-rolled HEA as base material (see Fig. 6c). The reason is the higher local ductility of the heat-treated HEA ($\epsilon_{HEA} = 23\%$) compared to the cold-rolled HEA ($\epsilon_{HEA} \sim 0\%$). As a result, the afore described global ductility of the cross-weld sample was improved.

3.6 Discussion of global DMW behavior vs. local fracture topography

Figure 8a shows a representative SEM figure of the fracture morphology of the DMW with the cold-rolled HEA, whereas Fig. 8b shows a magnified region of the weld joint mid thickness. The microvoid coalescence (MVC) morphology around the inclusions indicates high ductility of the respective microstructure. Figure 8c shows the SEM overview of the fracture topography of the DMW with the heat-treated HEA and Fig. 8d the magnified region. For both DMWs, the samples fractured in the intermixed WM. Interestingly, the MVC morphology changed and encompasses localized areas of quasi-cleavage (QC)-like patterns. That means despite the higher global deformability of the DMW with the heat-treated HEA compared to the cold-rolled HEA (19% vs. 13%, as shown in Table 4), the local deformation capability of the WM decreased.

The described DMW behavior (Sects. 3.4 and 3.5) is generally believed to be caused by highly different BM properties or the HAZ formation. In [35, 36], it was suggested that a weld joint can be regarded as a “composite material,” which deforms under iso-stress conditions during tensile loading. The problem is that the various local welding microstructures interact with each other and establish interdependencies in between. Hence, a focus on

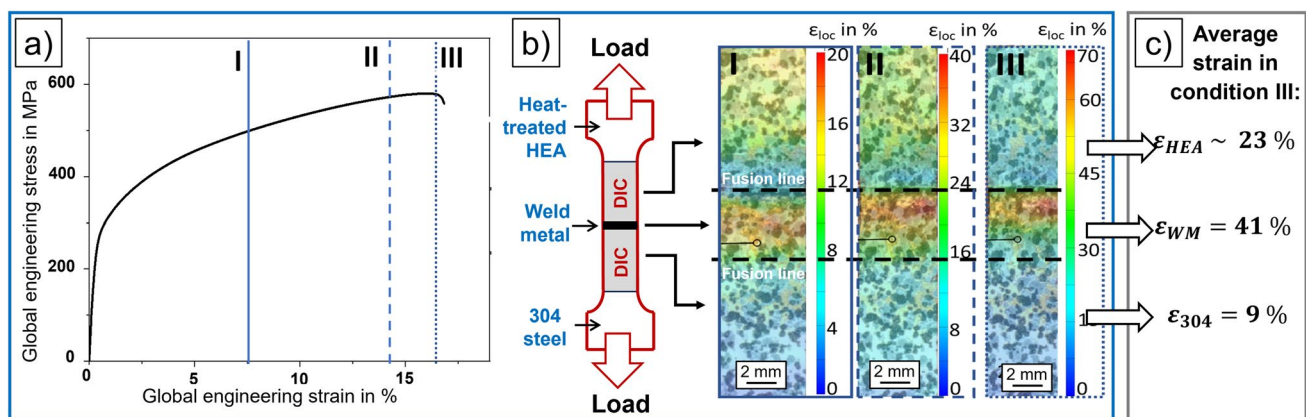


Fig. 7 Representative cross-weld tensile sample of DMW of heat-treated HEA welded to 304 steel: **a** global engineering stress strain curve, **b** local strains at load steps I to III

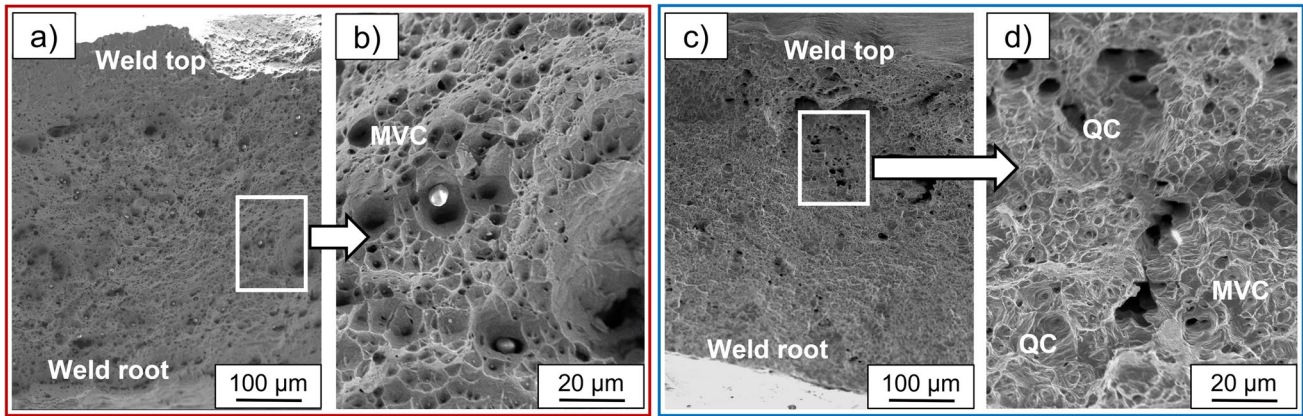


Fig. 8 SEM figures of fracture topographies of the DMW cross-weld tensile specimens of 304 steel welded to **a** HEA in cold-rolled condition, overview figure; **b** magnified center region of weld joint with

ductile/MVC morphology; **c** HEA in heat-treated condition, overview figure; and **d** magnified upper region of weld joint with MVC and QC morphology

merely global mechanical performance assessment of a cross-weld “blurs” the mechanical properties of the pure microstructures. Especially the hardening condition of a material (or excessive softening vice versa) can significantly influence the behavior if adjacent to a harder material. Reynolds et al. [35] hypothesize that the deformation of a material is limited by its surrounding, but less significant with increasing plastic deformation, the same behavior can be identified by the fracture topography in Fig. 8. The “hard” cold-rolled HEA results in merely ductile fracture (Fig. 8b) located in the intermixed WM. In contrast, the ductility of the intermixed WM is limited if the 304 steel is joined to the “soft” heat-treated HEA (as shown in Fig. 8d). Of course, the ratio width of the HAZ compared to the material thickness plays a significant role (in this study, approximately 4:1).

In addition, a more or less rigid surrounding adjacent microstructure has the same effect as a mechanical notch leading to a triaxial stress state [36], intensifying local differences in the mechanical properties. In other words, each material inhomogeneity can act like a geometric discontinuity. From that point of view, any discussion on local mechanical properties of a specific weld microstructures requires careful consideration of the surrounding microstructure.

Of course, this is not exclusively related to HEAs and their dissimilar metal welds as a weld joint represents a certain discontinuity in terms of both the metallurgical and the mechanical properties. For example, welded multi-material-mixes are state of the art especially in complex components like car bodies [37]. Nonetheless, basic weldability studies including cross-weld mechanical properties are of high interest in regard of this new HEA material. As shown in the next section, the application potential of a material is directly related to its weldability.

3.7 Perspectives for the application of CoCrNiFeMn-HEA-DMWs

The identified mechanical behavior (including the failure locations) suggests that the intermixed WM can be a potential crack susceptible region, for example, by mechanical overloading. Nonetheless, the presented cross-weld tensile properties (and the underlying microstructure assessment [28]) confirmed that the HEA can be joined by TIG to austenitic stainless steels like the 304 steel, showing sufficient mechanical performance in terms of strength and ductility. Nonetheless, a prior annealing of the HEA is beneficial in terms of the higher global ductility of the DMW (19% if joined to heat-treated HEA vs. 13% if joined to cold-rolled HEA, see Table 4). In general, the determined mechanical strength of the cross-weld tensile samples demonstrated the application potentials of a CoCrFeMnNi-based HEA. With respect to its desired properties, it could be of interest, e.g., as material for hydrogen applications, like high-pressure [38] or cryogenic storage [39] and in electrochemical corrosion environment [40, 41]. Although, distinct H₂ – applications for this material (especially in welded condition) are currently missing. Based on worldwide research efforts [5–8] and on recent results with the identical materials [21, 22, 28], it can be stated that welding of HEAs and its influence on the properties are of special interest for the near future.

4 Conclusions

HEAs will become of great interest as structural materials for the future due to their outstanding properties. Nonetheless, they encompass relatively expensive raw materials and synthesis. From that point of view, multi-material mixes

will be the state of the art and HEAs will have to be welded to different conventional materials. For that purpose, TIG welding experiments were carried out for the CoCrFeMnNi-HEA and a 304 steel as “conventional” counterpart for the DMW. To simulate different material processing conditions, the HEA was investigated in cold-rolled and heat-treated condition. The corresponding microstructure was characterized, hardness scans performed, and the local mechanical strains were characterized by digital image correlation (DIC-technique). The following conclusions can be drawn from the results presented:

- TIG welding allowed defect-free DMWs of CoCrFeMnNi-HEA joined to 304 steel. A prior heat treatment of the HEA significantly decreases the microhardness of the HEA.
- Nonetheless, both DMWs achieved sufficient mechanical properties in terms of the strength values. The DMWs generally have a remarkably decreased global ductility, whereas the heat-treated condition of the HEA resulted in somewhat better global ductility (19%) compared to the cold-rolled HEA (13%).
- The highest local strains were detected in the weld metal for both DMWs. The heat-treatment of the HEA caused a certain softening, which was responsible for decreased local strains in the WM of the corresponding DMW. Nonetheless, the high local strains caused the failure of the cross-weld samples always in the WM-region.
- The determined mechanical strength of the cross-weld tensile samples demonstrates the potentials of a CoCrFeMnNi-based HEA as structural material if welded to austenitic stainless steels.

Acknowledgements The HEA materials were kindly provided by Prof. G. Laplanche (Ruhr-University, Germany). The authors also thank Mr. A. Boerner and Mrs. M. Marten (both with BAM, Germany) for their assistance during the experiments. These were carried out as part of the BAM-project “Surface Degradation Mechanisms of Innovative Alloys” (SURDIA). Open-access publishing by “Projekt DEAL” is gratefully acknowledged.

Funding Open Access funding enabled and organized by Projekt DEAL. This research did not receive any specific grant from funding agencies in the public, commercial, or not-for-profit sectors.

Data availability The raw data is not accessible by the public but can be shared or be made available on demand with private access.

Declarations

Competing interests The authors declare no competing interests.

Open Access This article is licensed under a Creative Commons Attribution 4.0 International License, which permits use, sharing, adaptation, distribution and reproduction in any medium or format, as long as you give appropriate credit to the original author(s) and the source, provide a link to the Creative Commons licence, and indicate if changes were made. The images or other third party material in this article are included in the article’s Creative Commons licence, unless indicated otherwise in a credit line to the material. If material is not included in the article’s Creative Commons licence and your intended use is not permitted by statutory regulation or exceeds the permitted use, you will need to obtain permission directly from the copyright holder. To view a copy of this licence, visit <http://creativecommons.org/licenses/by/4.0/>.

References

1. Cantor B, Chang I, Knight P et al (2004) Microstructural development in equiatomic multicomponent alloys. *Mater Sci Eng A* 375–377:213–218. <https://doi.org/10.1016/j.msea.2003.10.257>
2. Yeh JW, Lin SJ (2018) Breakthrough applications of high-entropy materials. *J Mater Res* 33(19):3129–3137. <https://doi.org/10.1557/jmr.2018.283>
3. Heeger Materials (2023) Fe-Co-Ni-Cr-Mo spherical high-entropy alloy (HEA) powder. Heeger Materials Inc., St. Denver, CO, USA. Accessible via: <https://heegermaterials.com/spherical-powder/1490-spherical-refractory-high-entropy-alloy-powder-hea-fe-co-ni-cr-mo.html>. Accessed 2023–09–07
4. Stanford Advanced Materials (2023) DP3189 FeCrNiMnAl high-entropy alloy (HEA) spherical powder. Stanford Advanced Materials Inc., Lake Forest, CA, USA. Accessible via: <https://www.samaterials.com/fecrnmnal-high-entropy-alloy-hea-spherical-powder.html>. Accessed 2023–09–07
5. Rhode M, Richter T, Schroepfer D (2021) Welding of high-entropy alloys and compositionally complex alloys - an overview. *Weld World* 65:1645–1659. <https://doi.org/10.1007/s40194-021-01110-6>
6. Li J, Meng X, Wan L et al (2021) Welding of high entropy alloys: progresses, challenges and perspectives. *J Manuf Process* 68A:293–331. <https://doi.org/10.1016/j.jmapro.2021.05.042>
7. Lopes JG, Oliveira JP (2020) A short review on welding and joining of high entropy alloys. *Metals* 10(2):212. <https://doi.org/10.3390/met10020212>
8. Guo J, Tang C, Rothwell G et al (2019) Welding of high entropy alloys - a review. *Entropy* 21(4):431. <https://doi.org/10.3390/e21040431>
9. Carlone P, Astarita A (2019) Dissimilar metal welding. *Metals* 9(11):1206. <https://doi.org/10.3390/met9111206>
10. Fang Y, Jiang X, Mo D et al (2019) A review on dissimilar metals’ welding methods and mechanisms with interlayer. *Int J Adv Manuf Technol* 102(9–12):2845–2863. <https://doi.org/10.1007/s00170-019-03353-6>
11. Shen J, Goncalves R, Choi YT et al (2023) Microstructure and mechanical properties of gas metal arc welded CoCrFeMnNi joints using a 308 stainless steel filler metal. *Scripta Mater* 222:115053. <https://doi.org/10.1016/j.scriptamat.2022.115053>
12. Nam H, Park E, Chun EJ et al (2019) Laser dissimilar weldability of cast and rolled CoCrFeMnNi high-entropy alloys for cryogenic applications. *Sci Technol Weld Joining* 25(2):127–134. <https://doi.org/10.1080/13621718.2019.1644471>
13. Samiuddin N, Li J, Muzamil M et al (2022) Parametric optimization of diffusion welding process in joining of CoCrNi

- medium-entropy alloys (MEA) and SUS 304 stainless steel using full factorial design. *JOM* 74(11):4280–4293. <https://doi.org/10.1007/s11837-022-05500-z>
14. Oliveira JP, Shamsolhodaie A, Shen J et al (2022) Improving the ductility in laser welded joints of CoCrFeMnNi high entropy alloy to 316 stainless steel. *Mater Des* 219:110717. <https://doi.org/10.1016/j.matdes.2022.110717>
 15. Do H, Asadi S, Park N (2022) Microstructural and mechanical properties of dissimilar friction stir welded CoCrFeMnNi high entropy alloy to STS304 stainless steel. *Mater Sci Eng A* 840:142979. <https://doi.org/10.1016/j.msea.2022.142979>
 16. Adomako NK, Shin G, Park N et al (2021) Laser dissimilar welding of CoCrFeMnNi-high entropy alloy and duplex stainless steel. *J Mater Sci Technol* 85:95–105. <https://doi.org/10.1016/j.jmst.2021.02.003>
 17. Luo D, Xiao Y, Hardwick L et al (2021) High entropy alloys as filler metals for joining. *Entropy* 23(1):78. <https://doi.org/10.3390/e23010078>
 18. Disna Sahane KS, Singh S, Sivaprahasam D et al (2023) Investigation on high entropy alloys as interconnect material for intermediate temperature solid oxide fuel cells. *J Alloy Compd* 935(1):168000. <https://doi.org/10.1016/j.jallcom.2022.168000>
 19. Laplanche G, Volkert UF, Eggeler G et al (2016) Oxidation behavior of the CrMnFeCoNi high-entropy alloy. *Oxid Met* 85(5–6):629–645. <https://doi.org/10.1007/s11085-016-9616-1>
 20. Richter T, Schroepfer D, Rhode M et al (2022) Influence of machining on the surface integrity of high- and medium-entropy alloys. *Mater Chem Phys* 275:125271. <https://doi.org/10.1016/j.matchemphys.2021.125271>
 21. Richter T, Schroepfer D, Rhode M (2022) Residual stresses in a high- and a medium-entropy alloy due to TIG and friction stir welding. *J Manuf Mater Process* 6(6):147. <https://doi.org/10.3390/jmmp6060147>
 22. Richter T, Giese M, Rhode M et al (2022) Influence of surface preparation on cracking phenomena in TIG-welded high and medium entropy alloys. *J Manuf Mater Process* 6(1):5. <https://doi.org/10.3390/jmmp6010005>
 23. Strassburg FW, Wehner H (2009) Schweißen nichtrostender Stähle. DVS-Fachbücher No. 67, DVS-Verlag Düsseldorf, Germany, 4th ed
 24. DIN EN ISO 14175: Welding consumables - gases and gas mixtures for fusion welding and allied processes. German version of EN ISO 14175:2008. Beuth-Verlag, Berlin, Germany. <https://doi.org/10.31030/1401612>
 25. DIN 50159-1:2022: Metallische Werkstoffe - Härteprüfung nach dem UCI-Verfahren - Teil 1: Prüfverfahren (in German). English title: Metallic materials - hardness testing with the UCI method - Part 1: Test method. Beuth-Verlag GmbH, Berlin, Germany. <https://doi.org/10.31030/3346612>
 26. DIN EN ISO 6892-1: Metallic materials - tensile testing – part 1: method of test at room temperature. German version of EN ISO 6892-1:2019. Beuth-Verlag, Berlin, Germany. <https://doi.org/10.31030/3132591>
 27. Wu Z, David SA, Leonard DN et al (2018) Microstructures and mechanical properties of a welded CoCrFeMnNi high-entropy alloy. *Sci Tech Weld Join* 23(7):585–595. <https://doi.org/10.1080/13621718.2018.1430114>
 28. Richter T, Erxleben K, Rhode M et al (2023) Microstructure characterization of dissimilar metal welds of innovative high- and medium-entropy alloys to austenitic stainless steels joint by tungsten inert gas and friction stir welding. *Weld World* 1–9. <https://doi.org/10.1007/s40194-023-01618-z>
 29. Jin K, Sales BC, Stocks GM et al (2016) Tailoring the physical properties of Ni-based single-phase equiatomic alloys by modifying the chemical complexity. *Sci Rep* 6:20159. <https://doi.org/10.1038/srep20159>
 30. Saha J, Ummethala G, Malladi SRK et al (2021) Severe warm-rolling mediated microstructure and texture of equiatomic CoCrFeMnNi high entropy alloy: a comparison with cold-rolling. *Intermetallics* 129:107029. <https://doi.org/10.1016/j.intermet.2020.107029>
 31. Dan Sathiaraj G, Bhattacharjee PP (2015) Effect of cold-rolling strain on the evolution of annealing texture of equiatomic CoCrFeMnNi high entropy alloy. *Mater Charact* 109:189–197. <https://doi.org/10.1016/j.matchar.2015.09.027>
 32. Li DZ, Wei YH, Song JL et al (2014) Effect of heat-treatment temperature on the mechanical properties and microstructural evolution of cold-rolled twinning-induced plasticity steel. *J Wuhan Univ Technol - Mater Sci Ed* 30(2):386–391. <https://doi.org/10.1007/s11595-015-1157-y>
 33. ASTM A370–23: Standard methods and definitions for mechanical testing of steel products. 2017 Edition. ASTM International, West Conshohocken, PA, USA. <https://doi.org/10.1520/A0370-23>
 34. McGuire MF (2008) Stainless steels for design engineers. ASM International, Materials Park, OH, USA
 35. Reynolds AP, Duvall F (1999) Digital image correlation for determination of weld and base metal constitutive behavior. *Weld J* 78(10):355-s-360-s
 36. Hertzberg RW, Vinci RP, Hertzberg JL (2012) Deformation and fracture mechanics of engineering materials. Wiley & Sons Ltd, New York, USA, 5th ed
 37. Abdul Karim M, Park YD (2020) A review on welding of dissimilar metals in car body manufacturing. *J Weld Join* 38(1):8–23. <https://doi.org/10.5781/JWJ.2020.38.1.1>
 38. Zhao Y, Lee DH, Seok MY et al (2017) Resistance of CoCrFeMnNi high-entropy alloy to gaseous hydrogen embrittlement. *Scripta Mater* 135:54–58. <https://doi.org/10.1016/j.scriptamat.2017.03.029>
 39. Luo H, Lu WJ, Fang XF et al (2018) Beating hydrogen with its own weapon: nano-twin gradients enhance embrittlement resistance of a high-entropy alloy. *Mater Today* 21(10):1003–1009. <https://doi.org/10.1016/j.mattod.2018.07.015>
 40. Rhode M, Wetzel A, Oczan O et al (2020) Hydrogen diffusion and local Volta potential in high- and medium-entropy alloys. *IOP Conf Ser: Mater Sci Eng* 882:012015. <https://doi.org/10.1088/1757-899X/882/1/012015Richter>
 41. Luo H, Li ZM, Mingers AM et al (2018) Corrosion behavior of an equiatomic CoCrFeMnNi high-entropy alloy compared with 304 stainless steel in sulfuric acid solution. *Corros Sci* 134:131–139. <https://doi.org/10.1016/j.corsci.2018.02.031>

Publisher's Note Springer Nature remains neutral with regard to jurisdictional claims in published maps and institutional affiliations.